Accepted Manuscript

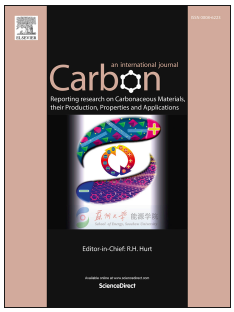

A time-dependent atomistic reconstruction of severe irradiation damage and associated property changes in nuclear graphite

Baptiste Farbos, Helen Freeman, Trevor Hardcastle, Jean-Pierre Da Costa, Rik Brydson, Andrew J. Scott, Patrick Weisbecker, Christian Germain, Gérard L. Vignoles, Jean-Marc Leyssale

PII: S0008-6223(17)30454-2

DOI: 10.1016/j.carbon.2017.05.009

Reference: CARBON 11996

To appear in: *Carbon*

Received Date: 9 March 2017

Revised Date: 28 April 2017

Accepted Date: 4 May 2017

Please cite this article as: B. Farbos, H. Freeman, T. Hardcastle, J.-P. Da Costa, R. Brydson, A.J. Scott, P. Weisbecker, C. Germain, Gé.L. Vignoles, J.-M. Leyssale, A time-dependent atomistic reconstruction of severe irradiation damage and associated property changes in nuclear graphite, *Carbon* (2017), doi: 10.1016/j.carbon.2017.05.009.

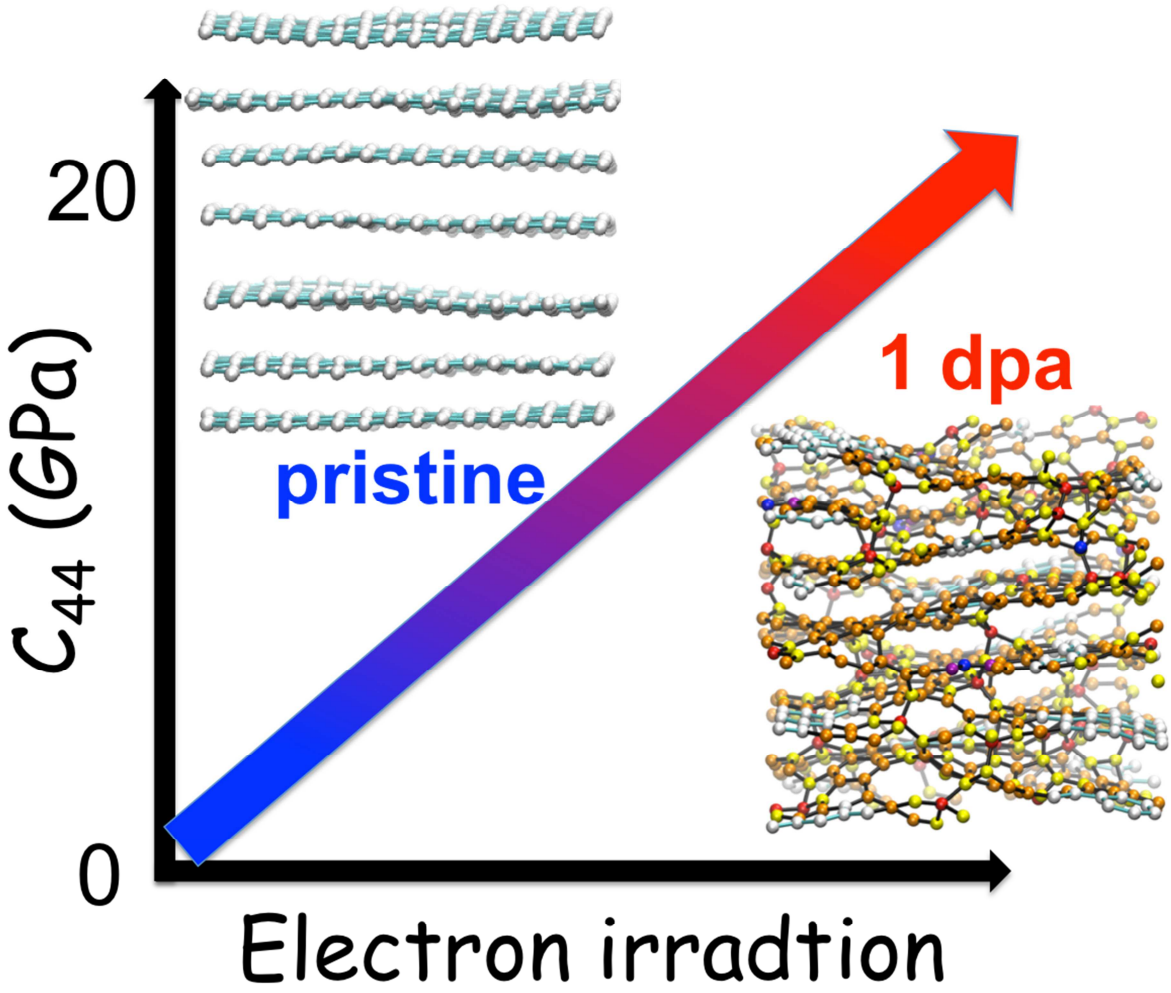

A time-dependent atomistic reconstruction of severe irradiation damage and associated property changes in nuclear graphite

Baptiste Farbos[a,b], Helen Freeman[c], Trevor Hardcastle[c], Jean-Pierre Da Costa[b], Rik Brydson[c], Andrew J. Scott[c], Patrick Weisbecker[a], Christian Germain[b], Gérard L. Vignoles[a], Jean-Marc Leyssale[a,d,*]

[a] *Laboratoire des Composites ThermoStructuraux, Université de Bordeaux - CNRS - CEA - Safran Ceramics, 33600 Pessac, France*
[b] *Université de Bordeaux, IMS UMR 5218, F-33400 Talence, France*
[c] *Institute for Materials Research, School of Chemical and Process Engineering, Univiversity of Leeds, Leeds LS2 9JT, UK*
[d] *MultiScale Material Science for Energy and Environment, Massachusetts Institute of Technology - CNRS, 02139 Cambridge MA, USA*

Abstract

Detailed knowledge regarding the nature of and mechanisms causing neutron irradiation damage in graphite remains a scientific and technological challenge, particularly at high irradiation doses. Using electrons as a surrogate for neutron irradiation, we develop a time-dependent atomistic reconstruction strategy fed by a time series of high-resolution transmission electron microscopy (HRTEM) images, to monitor damage propagation in a graphite grain up to a dose of about one displacement per atom (*i.e.* well beyond the conventional irradiation simulations based on molecular dynamics). The reduction in crystalline order and the development of interlayer bonding observed in the models with increasing irradiation time induce significant mod-

*Corresponding author
Email address: leyssale@lcts.u-bordeaux.fr (Jean-Marc Leyssale)

ifications of the elastic constants and thermal conductivity. Homogenizing these properties to the case of isotropic polycrystalline graphite we are able to reproduce the increase in Young's modulus and decrease in thermal conductivity observed experimentally for reactor graphites with increasing dose. Further validation of the models is provided via a comparison of simulated and experimental data from irradiated material such as: HRTEM images, carbon K-edge electron energy loss spectra, dose rate and stored energies.

1. Introduction

Controlled nuclear fission has always been intimately linked to graphite, from the first nuclear piles in the 1940s, through the first civil nuclear reactor, Calder Hall, which opened in 1956, and subsequent second and third generation reactors (Magnox and Advanced Gas-Cooled Reactors (AGR), to the next generation (GenIV) very high temperature reactors (VHTR). In most designs, graphite serves not only as a neutron moderator but also as a key structural component, providing the mechanical integrity of the core, and acting as a thermal management system. As an example of the importance of graphite in the field, over 90 % of the current nuclear reactors in the UK are based on a graphite core. Knowledge of radiation damage and its effects on properties in nuclear graphite is thus particularly important at a time where society has to make important choices related to the extension or decommissioning of existing, older nuclear reactors, as well as the development of new high temperature reactors.

Neutron radiation produces atomic displacement cascades in graphite, reducing crystalline order to only a few nm [1] and resulting in contraction along

the a-axis and swelling along the c-axis [2, 3] also observed upon electron irradiation [4]. Even though graphite core reactors usually operate at high temperature (≈ 400°C), it is often more convenient to study radiation effects at room temperature to avoid thermal annealing of the produced damage. From the point of view of physical properties, increases in Young's modulus (E) by factors of two [5] to four [6], due to an increase in C_{44} in graphite grains [7], as well as decreases in thermal conductivity (κ) by approximately an order of magnitude [8] have been reported for nuclear graphites upon neutron irradiation at room temperature.

Using DFT calculations, Heggie *et al.* have ascribed dimensional changes to the buckling of graphene layers induced by interlayer defects (spiro-interstitials) [9, 10] in addition to the growth of vacancy lines and interstitial prismatic loops as previously hypothesized [11, 12]. Direct molecular dynamics (MD) simulations of the impact of energetic particles on graphite [13–17] tend to confirm the formation of pinned interstitial atoms. However, these theoretical and simulation studies are limited to primary damage, in which only a small fraction of the atoms are displaced (10^{-2} in Ref. 17), in contrast to doses of 20-30 displacements per atom (dpa) experienced by nuclear graphite components. Constructing structural models of graphite at higher irradiation doses and rationalizing them with the experimental observations of pronounced changes in physical properties is therefore a key issue for the development of new reactors, the assessment of the optimal life time of actual plants or the decommissioning of older ones.

Reconstructive atomistic modeling methods have proven to be considerably helpful in the elucidation of structure-property relationships for various

carbonaceous materials [18–21]. In particular, the image guided atomistic reconstruction (IGAR) method, using high resolution transmission electron microscopy (HRTEM) images as input data, has allowed the construction of atomistic representations of highly anisotropic pyrolytic carbons reproducing with great accuracy both experimental textural (HRTEM images) and structural (pair distribution functions) data [21, 22].

Building up on former experimental work [4, 23, 24] showing that electron and neutron irradiation damage can be compared, we present in this work a time-dependent IGAR method to model the propagation of radiation damage in graphite using as experimental input a series of HRTEM images taken during *in situ* electron irradiation of graphite. Irradiation induced changes in physical properties are then discussed based on the proposed models.

2. Materials and methods

2.1. Transmission electron microscopy

TEM samples of Pile Grade A (PGA) graphite were prepared by grinding/crushing. Flakes were mixed with acetone and dispersed onto 3 mm copper TEM grids coated with holey amorphous carbon support film; the areas examined were < 50 nm thick. *In situ* TEM studies were performed in a Philips CM200 field emission TEM operated at 200 kV with a tip extraction bias of 3.21 kV and equipped with a GIF200 EELS spectrometer. We operated at Scherzer defocus c.a. -698 Å and data were collected periodically (every 1 min.) during room temperature electron beam exposure over several regions within the specimen. The localized heating effect from the electron beam was considered to be negligible due to the high thermal conductivity of

graphite. The total duration of the exposure was of 13 minutes, which corresponds to a total estimated dose of around 1 dpa (see below). Considering that actual reactor dose rates are on the order of 1 dpa per 15 months of operation at full power and that significant annealing occurs under operation temperatures, the damage level corresponding to 1 dpa of room temperature electron irradiation should be equivalent to the one obtained in a reactor core after a few years of its lifetime.

2.2. Time-dependent image guided atomistic reconstruction

The principles of the IGAR method, introduced in Ref. 25 and further developed in recent years [21, 22], are schematized in Fig. 1(a). It starts with the production of a 3D HRTEM image block, from an initial random distribution of grey levels, using a multi-resolution pyramidal image synthesis technique trained to reproduce image statistics collected on 2D images and extended to 3D by considering the equivalence of spatial statistics by rotation around the c axis. In a second step, this 3D analogue of the 2D experimental HRTEM image is used as an external potential in a liquid quench MD simulation to guide atoms towards regions inferred from HRTEM fringes to be high atomic density. At the end of the quench, the resulting atomistic model is both chemically sound, thanks to the used interatomic potential, and carries the nanotexture of the actual material, thanks to the HRTEM template. This method has proven successful in the elucidation of the nanostructure of highly textured laminar pyrocarbons [21].

We present in Fig. 1(b) a modification of this method, the time-dependent IGAR method (TD-IGAR), specifically developed in this work to model the dynamic evolution of an anisotropic carbon from a given time series

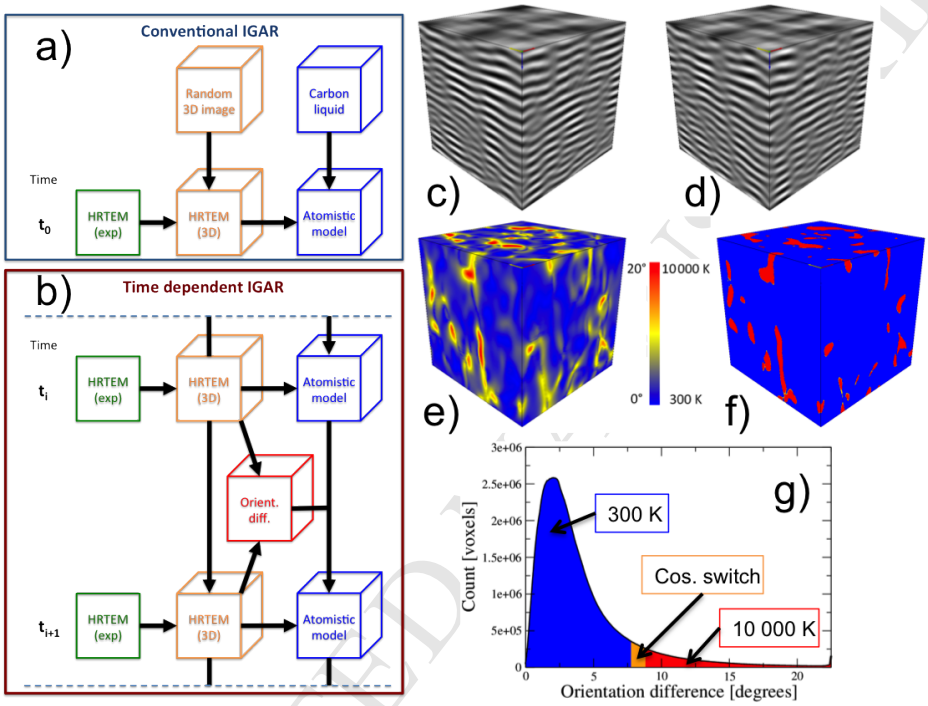

Figure 1: Schematic description of (a) the conventional IGAR method and (b) the time-dependent IGAR method. (c,d) 3D HRTEM image analogues at (c) 4 and (d) 5 minutes of irradiation. (e) Image of the orientation difference (OD) between the 3D images at 4 and 5 min. (f) Initial temperature image for the reconstruction of the atomistic model at 5 min of irradiation. (g) histogram of the OD image (e) showing the three regimes of initial temperatures (in the orange domain a cosine function is used to progressively increase temperature with OD from 300 K to 10 000 K).

of HRTEM images. The starting points here are a pre-existing 3D HRTEM image block and an atomistic model of the system at a given time t_i (for instance produced by a conventional IGAR simulation). Then, a 3D HRTEM image at time t_{i+1} is obtained by modifying the 3D HRTEM image at time t_i in order to match the statistics derived from the experimental 2D image at time t_{i+1}. The pyramidal 3D synthesis, being based on a local optimization scheme, ensures that the produced block at t_{i+1} is a minimal perturbation from the block at time t_i (see examples of two such blocks corresponding to 4 and 5 min of electron irradiation in Fig. 1(c) and Fig. 1(d), respectively). Similarly, the 3D atomistic model at time t_{i+1} is obtained by modifying the atomistic model at time t_i, however, special care need to be taken such that only damaged areas get altered, or in other words, areas in which the 3D image block has significantly changed between time t_i and time t_{i+1}. In order to do identify such areas, an orientation difference (OD) image (Fig. 1(e)) is produced from the angular difference between the normal to the grey-level iso-surface at a given location at times i and $i+1$. The normal vector is estimated on every voxel of the 3D HRTEM image using the structure tensor technique [26]. This 3D OD image is converted (see Fig. 1(g)) into a 3D temperature image block (Fig. 1(f)): 10,000 K and 300 K for OD larger and lower than some upper and lower thresholds respectively, with a cosine switch in between. This temperature image block then serves to define the space-dependent initial temperature for a rapid MD quench run. The latter starts with the atomistic model at time t_i and is biased by the HRTEM image at time t_{i+1}. The result from this run is the atomistic model at time t_{i+1} in which changes in chemical bonding can only have occurred in areas of high

OD values.

2.3. Evaluation of elastic properties and thermal conductivities

Elastic constants (and compliances) at room temperature and finite strains are obtained using relaxed tensile simulations, constrained tensile simulations and shear simulations under Lees-Edwards [27] boundary conditions as described in Ref. 28. Engineering strain rates are set to 0.4 and 1 ns^{-1} for tensile tests and shear tests, respectively. Phonon contributions (in the classical limit) to the thermal conductivities are computed using the velocity-swapping NEMD scheme of Müller-Plathe [29]. In these simulations, the systems are replicated three times along the test direction to limit the magnitude of the temperature gradients. One velocity swapping event was performed every 12.5 fs and 50 fs for simulations along a and c directions, respectively. This leads to gradients of the order of 3-5 (a) K/nm and 20-25 K/nm (c).

2.4. Computational details

Molecular dynamics simulations are performed on periodic cubic cells of 5.025 nm width filled with 14009 carbon atoms (*i.e.* at a fixed density of 2.2 $g.cm^{-3}$). Interatomic interactions are accounted for by the second generation reactive empirical bond order potential (REBO) [30], which provides a reasonable description of defect energies in graphite [31, 32] and has been recently used to investigate primary damage in graphite [17] and the structure/property relationships of many graphite-based materials [18, 19, 28]. Van der Waals interactions between non-bonded carbon atoms, not included in the IGAR quenches, are introduced in order to relax the systems after removal of the image potential and to compute properties. This is achieved

using a Lennard-Jones potential introduced in an adaptive way based on both distance and bond order criteria [33]. Equations of motion are integrated with a velocity-Verlet integrator with time steps of 0.25 fs for simulations involving high temperatures (IGAR and TD-IGAR reconstructions) and 0.5 fs for simulations performed at room temperature (relaxations and property evaluations). The stochastic Andersen thermostat [34] is used to fix the temperature in most simulations. The only exception is the non-equilibrium MD (NEMD) simulations to evaluate thermal conductivities, for which a Berendsen thermostat [35] is used. In this particular case the thermostat only aims at avoiding energy drifts on long timescale runs. The time constant of the thermostat was thus set to a large value (0.5 ps) in order to have little effect on the obtained temperature gradient, which was checked against shorter Newtonian runs. In some simulations (constant pressure relaxations and relaxed tensile tests), all or some diagonal elements of the stress tensor are fixed to atmospheric pressure using an anisotropic Berendsen barostat [35].

The 3D HRTEM image blocks used as external potentials in the (TD-)IGAR reconstructions have a 9.81 pm/pixel resolution and were synthesized from data collected on experimental images at least 25 nm and 10 nm width along the a and c directions, respectively. The proportionality relationship between energy and grey level is as in former work [21]: from 0 eV (black) to 4 eV (white). This correspondence between dark contrasts and high atomic density was verified using HRTEM simulation for atomistic models as wide as 12.5 nm [21].

The initial atomistic model in the TD-IGAR process is built from the HRTEM image obtained at two minutes of irradiation (lower irradiation times

could not be accurately described by the 5 nm width models used in this work) using almost the same simulation parameters as those given in Ref. 21. The only difference is that the minimum quench rate is reduced by a factor of 2, down to 0.25 K/ps, at temperatures between 5,200 and 4,000 K.

In the TD-IGAR approach, the initial temperature T_{init} for the quench process is non-uniform in space; it depends on the difference in orientation (OD) at a given location between the actual 3D HRTEM-like image block and the one at the former step. Based on tests of the effects of simulation parameters on the reproduction of HRTEM features we adopted the following choice of parameters: T_{init} was set to 300 K and 10,000 K at respectively low and high OD with a cosine switch in between (see Fig. 1(g)). The threshold OD values for low and high T_{init} were chosen so that they belonged to the tail of the OD histogram, whose precise location showed some slight difference from one system (*i.e.* one time) to another. On average we used $T_{init} = 300$ K for $OD < 7.5°$ and $T_{init} = 10{,}000$ K for $OD > 8.5°$ (note that this choice is not that sensitive as, owing to the very rapid quench rate, structural changes will only occur where strong alterations of the 3D HRTEM image blocks have taken place, in other words, far into the tail of the OD histogram). As in former work, the IGAR and TD-IGAR runs are performed without the van der Waals potential to save computational time. The latter is introduced in a second step to relax the system before property calculations are undertaken.

2.5. HRTEM simulation

HRTEM images were simulated from the atomistic models using the multislice image simulation technique implemented in the NCEMSS package [36]. The microscope parameters were set to match the experimental study. Two

images were simulated for each atomistic model, with the electron beam aligned with the two equivalent directions (a and b axes). Average image properties (L_2, τ, RIMOD) were computed based on these two sets of images.

2.6. EELS calculations

A small-scale (216 atoms) atomistic model was produced using a simple liquid quench MD simulation to allow for the calculation, using density functional theory (DFT), of C K- electron loss near edge structures (ELNES). The system density, 2.0 g/cm^{-3}, and the quench rate, 0.25 K/ps, were chosen so as to produce a structure resembling as much as possible that of the larger irradiated graphite models. It is worth noting that, in such a small system, highly anisotropic carbon forms straightforwardly and without imposing any bias such as the external potentials based on 3D HRTEM image blocks used in the IGAR simulations, because of the strong interactions with the periodic boundary conditions.

ELNES features of this model were computed using the plane wave DFT [37, 38] code CASTEP [39] with the Tkatchenko-Scheffler-van der Waals-corrected [40] GGA PBE [41] functional with a 4×4×4 Monkhorst-Pack [42] k point grid (spacing of less than 0.022 Å^{-1}), and a plane wave energy cut-off of 600 eV. The model was fully relaxed before calculation of the carbon K-edges using 3072 unoccupied states up to +65 eV above the Fermi energy with self-consistently generated [43] on-the-fly pseudopotentials where Blöchl's projector-augmented wave [44] (PAW) formalism was used to reconstruct the all-electron eigenstates to calculate the matrix elements. The scattering momentum change $\overrightarrow{q}$ in the perturbation term $e^{i\overrightarrow{q}.\overrightarrow{r}}$ was neglected to

satisfy the dipole approximation in keeping with the small collection aperture semi-angle used in the experiment. Energy-independent Gaussian instrumental broadening of 0.7 eV was applied alongside Lorentzian final-state lifetime broadening of 0.17 eV based on published values [45].

3. Results

3.1. HRTEM observation

Three HRTEM (002) lattice fringe images taken from the 14 images time series are presented in Fig. 2(a-c). At short irradiation times (2 min), long linear fringes, reminiscent of the virgin (unirradiated) graphite structure, are easily detected in the images. However, fringes exceeding 3 nm length are very rare at the end of the 13 minute irradiation process as shown in the filtered images with superimposed fringes in Fig. 2(d-f)). The overall fringe tortuosity also significantly increases with increasing irradiation time as can be visually perceived from these images. Damage progression is also evident in the orientation images (Fig. 2(g-i)) where large columnar domains of even contrast and hence constant orientation are observed at short irradiation times, whilst smaller patchy orientation domains can be observed at the end of the process. A complete time series of rotated HRTEM image cuts is given as supporting movie S1 and quantitative descriptions of fringe (Fig. S1) and orientation (Fig. S2) properties are provided in section S1 of the supplementary material.

3.2. Atomistic models of irradiated graphite

We now present the properties of the times series of atomistic models, dynamically reconstructed with the TD-IGAR method, based on data gath-

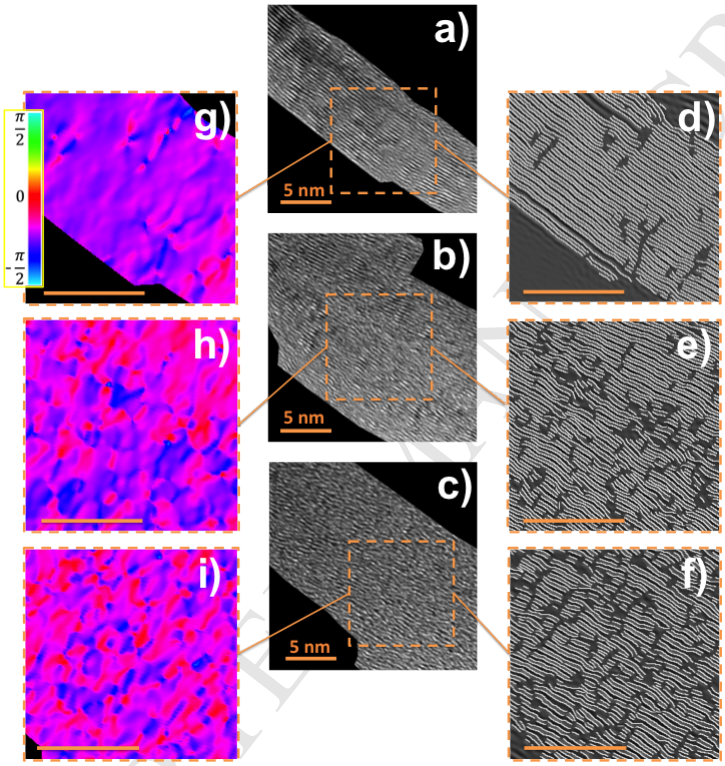

Figure 2: HRTEM images of graphite during in-situ electron irradiation. (a-c) Observed (002) lattice fringes after (a) 2, (b) 6 and (c) 13 minutes of irradiation. (d-f) Band pass filtered enlargements of (a-c) with superimposed fringes. (g-i) orientation images of (d-f). Image analysis was limited to domains having their 002 direction normal to the electron beam, other areas are masked in black.

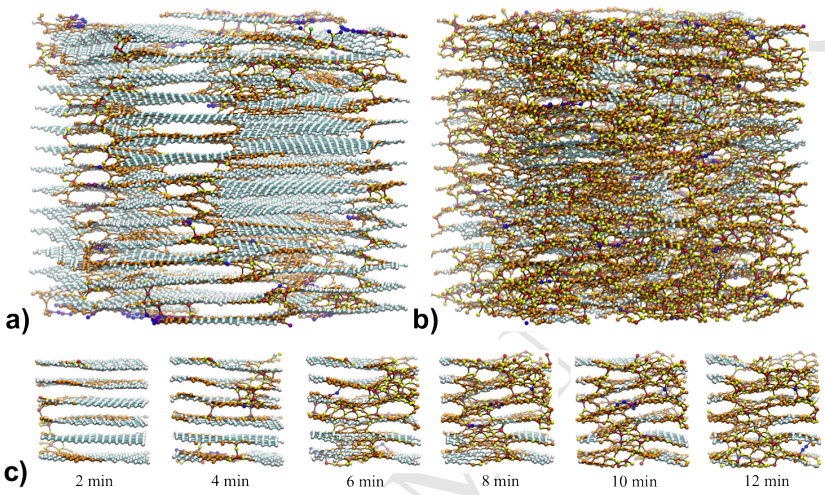

Figure 3: Full size atomistic models of electron irradiated graphite after (a) two and (b) thirteen minutes of irradiation. (c) time series of atomistic models by steps of two minutes (only 2×2×2 nm^3 volumes are displayed for clarity). Atoms are color coded according to C_6 (threefold atom in three hexagonal rings) : white; C_4 (fourfold atom): red; C_{3a} (threefold atom bonded to three threefold atoms, yet belonging to a non-hexagonal ring): orange; C_{3b} (threefold atom bonded to at least one fourfold atom): yellow; C_{3c} (threefold atom bonded to at least one twofold or singlefold atom): violet; C_2 (twofold atom): blue; C_1 (onefold): green; bonds between two C_6: cyan; other bonds: black (see text for the definition). The full time series of snapshots is also provided as movies S2 ($2 \times 2 \times 2$ nm^3 volumes) and S3 (full width, 1 nm thick slabs).

ered from the HRTEM images. Some of them are presented as snapshots (either full sized or small volume cuts) in Fig. 3; the distribution of chemical environments within these models is described in Fig. 4.

The initial model, reconstructed using the usual IGAR method from the HRTEM image of graphite after two minutes of electron irradiation is shown in Fig. 3(a). This model essentially retains a graphite-like structure with more than 98 % of the atoms being threefold coordinated (sp^2) and more than 70 % (see Fig. 4), denoted as C_6 atoms in the present work, belonging to three distinct hexagonal rings (see Fig. 3(c)). Among the remaining 30 % of "defect" atoms are a few fourfold (sp^3) and twofold (either sp or edge-radical sp^2) coordinated atoms denoted as C_4 (0.9 %) and C_2 (0.6 %), respectively, as well as 28 % of defective sp^2 atoms. The latter can be subdivided into atoms bonded only to sp^2 atoms yet belonging to a non-hexagonal ring, denoted as C_{3a} (24 %), atoms bonded to a C_4 atom, denoted as C_{3b} (3 %) and the remainder of sp^2 atoms (those bonded to two-fold (C_2) or single-fold (C_1) atoms), denoted as C_{3c} (less than 1 %). C_6 atoms form large, well-stacked graphene domains resulting in relatively long pair correlations and narrow diffraction peaks (see Fig. S4 in the supplementary materials), corresponding to relatively large coherence lengths (L_a = 4.0 nm, L_c = 4.6 nm) compared to the simulation cell (a 5 nm wide cube). The interlayer distance between the basal planes, d_{002}, is equal to the value in pristine graphite (0.335 nm), even though our model adopts a turbostratic stacking of basal planes, due to random in-plane orientations, inherent to the reconstruction technique. Hexagonal graphene layers are bound in plane through well-known grain boundaries involving pentagonal and heptagonal rings [22, 46], giving rise to

C_{3a} atoms. In addition, a complex network of interlayer crosslinks, essentially in the form of screw dislocations, as identified recently in pyrolytic carbons [22] and predicted to be a stable defect in graphite using DFT calculations [47, 48], is clearly visible in Fig. 3(a). This is where most C_4, C_{3b} and C_{3c} atoms are apparent, in addition to numerous C_{3a} atoms.

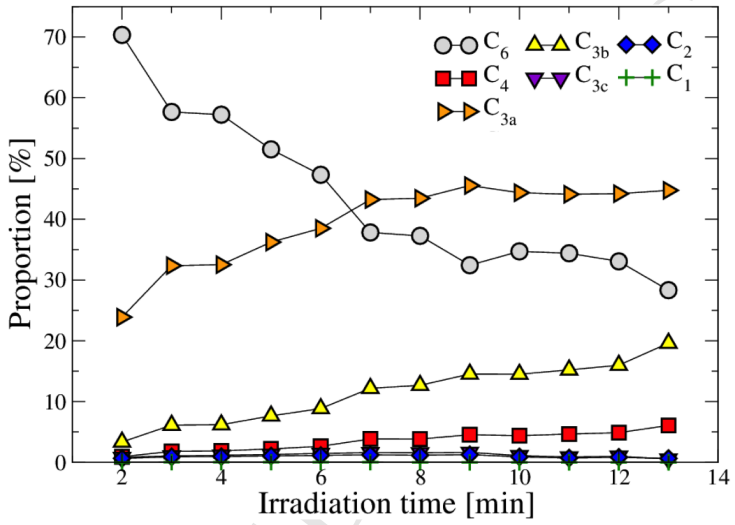

Figure 4: Evolution with irradiation time of the proportions of the different atomic carbon environments (same definition and color code as in Fig. 3).

Fig. 3(c) and Fig. 4 reveal that under further irradiation, up to 13 min, the total fraction of sp^2 atoms slightly decreases from 98 % down to 93 %, which is essentially accounted for by an increase in sp^3 (C_4) atoms, from 0.9 % up to 6 %, the C_2 fraction remaining at around 1 % during the whole process. With increasing irradiation the fraction of C_6 atoms is significantly reduced, from above 70 % down to 28 %, while the fraction of C_{3a} atoms increases from 24 % up to 45 % due to a significant increase in the number of non-hexagonal rings, essentially pentagons and heptagons (see table S1 for

detailed ring statistics). Correspondingly the fraction of C_{3b} atoms increases from 3 % to about 20 %, yet the ratio of C_{3b} to C_4 atoms remains in the range 3.2 to 3.6, indicative of a very limited clustering of C_4 atoms. We note, that the production of defects (mainly C_4, C_{3a} and C_{3b} atoms), rapid in the very beginning of the process, tends to saturate above 9 min of irradiation. Because of the large amount of damage occurring between two successive models (see the dose rate below) we cannot assess the atomistic details of damage production. However, as shown in Fig. 3(c), this work provides for the first time a clear picture of damage progression at larger scale. The reduction of in-plane order and increase in layer buckling is evident and consistent with the significant decrease of intensity in the long range pair correlation functions and reduction in longitudinal and transverse coherence lengths (see Fig. S4). Also evident in Fig. 3(c) is the nucleation and build-up of the screw dislocation network.

3.3. Validation

In Fig. 5 we compare some properties of experimental HRTEM images and images derived from the 3D atomistic models obtained using a multi-slice HRTEM simulation software [36]: L_2, the average fringe length (Fig. 5(a)); β^{MOD}, the plateau value of the rotationally invariant mean orientation difference (RIMOD) [49] at large (inter-domain) distances (Fig. 5(b)); and L^{MOD}, the average pixel to pixel distance at a fixed intra-domain RIMOD value (Fig. 5(c)). As can be seen, the simulated HRTEM images reproduce the evolution with irradiation of the fringe and orientation properties observed in experimental images. The only significant deviation is observed for β^{MOD} values at longer irradiation times, indicating a slight overestimation

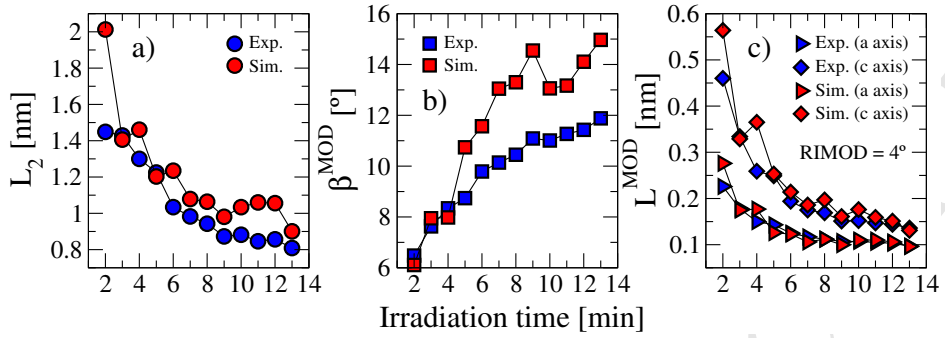

Figure 5: Quantitative comparison of simulated and experimental HRTEM images. Evolutions with irradiation time of (a) the average fringe length L_2, (b) the plateau value β^{MOD} of the RIMOD at large interpixel distance, and (c) the average interpixel distance at which RIMOD = 4°. Fringes with $L_2 > 4$ nm were discarded from the analysis in (a) to allow for a comparison between simulations and experiments. The complete time series of simulated HRTEM images are available as supporting movies S4 and S5.

of the misorientation between adjacent orientation domains. Comparison of experimental (Fig. S2(c)) and simulated (Fig. S3(b)) isovalue polar chats of the RIMOD, in the supplementary materials, further validate the reproduction of image properties.

The dose rate, expressed as the number of displacements per atom (dpa) and per unit time can be relatively easily calculated from the models. For this, we considered successive models (*i.e.* separated by a one-minute time interval) and used two criteria for atomic displacements: one based on a minimum displacement distance of 1.42 Å, corresponding to the bond length in graphite, and the second one based on a minimum change of connectivity of at least two neighbors, which holds for the creation (or annihilation) of all common defects (Stone-Wales, vacancy, interstitial, etc...). These two criteria led to very similar results for the number of displaced atoms at each

step (less than 5% difference between the two methods) and the same average dose rate: 0.070 dpa/min (see Fig. 6).

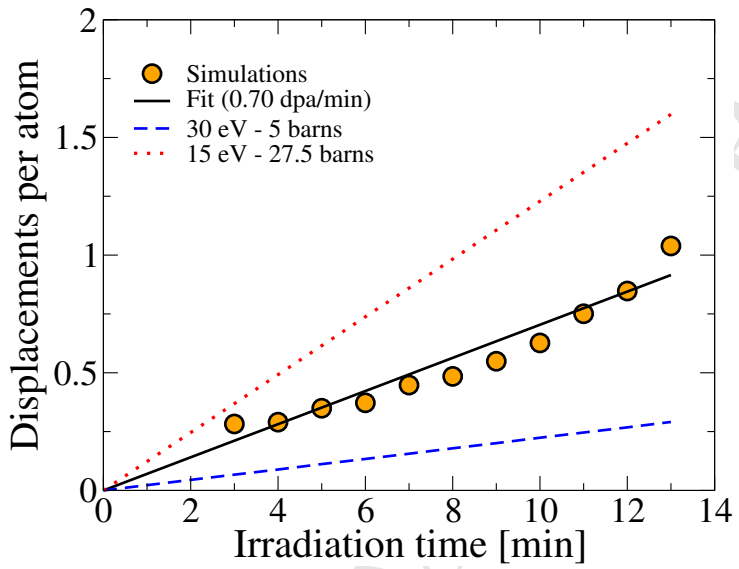

Figure 6: Cumulative number of displaced atoms (expressed in dpa) as a function of irradiation time. Symbols: simulation results (uncorrected for multiple displacements) using the connectivity criterion (the data were shifted, based on fit, to match a zero displacement at the unirradiated stage); full line: linear fit to the simulation data; dashed blue line: lower limit of the experimental dose based on $E_d = 30$ eV, corresponding to $\sigma_d = 5$ barns [50, 51]; red dotted line: upper limit based on $E_d = 15$ eV ($\sigma_d = 27.5$ barns) [51, 52].

However, our method for the dose calculation does not account for the possibility that an atom undergoes several (two) displacements between two successive models and thus provides a lower limit of the dose rate. A correction to account for double displacement, $q^2/2 = 0.00245$ where q is the calculated dose rate (this was obtained by integrating over one minute the number of displaced atom at time t multiplied by the displacement proba-

bility of an atom in a time interval δt) allows obtaining a corrected dose rate of 0.072 dpa/min from the MD simulations. The total dose corresponding to the 13 minutes exposure is thus estimated to 0.94 dpa. We would also like to stress that this correction term only represents a small fraction of the total dose rate, thus validating the choice of a one minute interval between two successive snapshots.

In the TEM experiment, the average electron flux during beam exposure was approximately 7.85×10^5 nm^{-2}s^{-1}, which, for a 13 minutes long exposure, gives a total fluence of 5.81×10^8 e$^-$ nm^{-2}. The conversion from electron fluence to displacements per atom can be calculated by considering the displacement cross section (σ_d) and energy displacement threshold of a carbon atom (E_d). There has been a relatively broad range of E_d values quoted in the literature for various graphite-related structures, basically from 10 to 60 eV [50, 52], confusing the issue of the conversion between electron fluence and dose. However, most recent studies, either based on experiments or calculations seem to converge towards a narrower range of 15 to 30 eV [14, 16, 50, 51, 53–55].

Assuming 30 eV and 15 eV as upper and lower bounds for E_d, an electron energy of 200 kV, and referring to Ref. 56 we obtain lower and upper bounds for σ_d of 5 and 27.5 barns, respectively. The corresponding dose rates, which we consider here as lower and upper bounds (see Fig. 6), are thus of around 0.0225 and 0.123 dpa/min, respectively. We see that the dose rate determined from the models, 0.072 dpa/min, resides almost exactly in the middle of the experimental uncertainty. It corresponds to an energy displacement threshold of around 20 eV, *i.e.,* very close to recent estimations for graphene (21 eV

using TEM and DFT [55]) and graphite (25 eV using MD simulations [16, 50]). A last point to mention here is that, for simplicity and because of lack of available data, we have considered here that the dose is a linear function of irradiation time (or electron fluence). However, after severe irradiation damage one can expect the energy displacement threshold to become reduced [57], and hence, exhibit an increase in dose rate with increasing irradiation time, as seems to be the case in the simulation data (see Fig. 6).

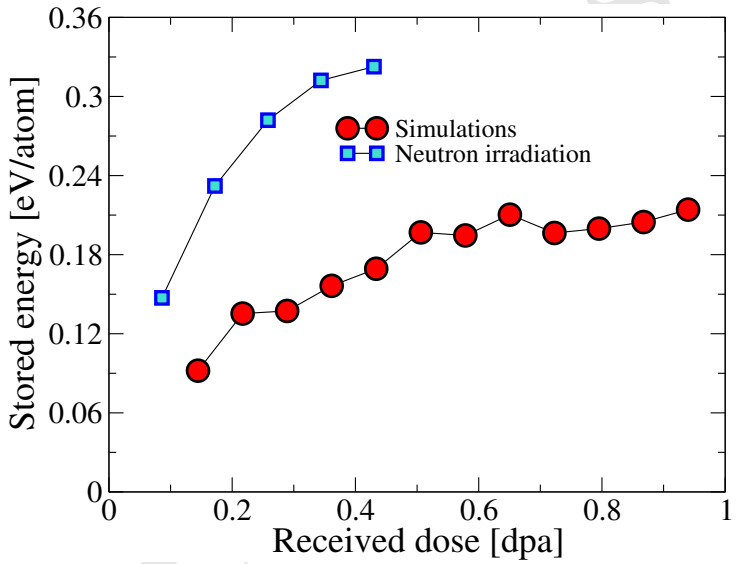

Figure 7: Stored energy of the irradiated graphite models as a function of the received dose. Heat of combustion measurements for graphite irradiated with neutrons at room temperature are given for comparison [58].

The amount of energy stored by the material during irradiation (*i.e.* its net change in enthalpy) is a crucial and well-characterized property of nuclear graphites as this energy could be released upon accidental increase in temperature and potentially promote melting of the fission reactor core (Wigner effect). We present in Fig. 7 the evolution with dose of the stored energy,

computed as the average atomic enthalpy difference between irradiated and pristine graphite models at room temperature and zero pressure. We observe a sharp increase at the beginning of the irradiation process up to a plateau of about 220 meV/atom obtained at around 0.6 dpa (corresponding to ≈ 9 min of irradiation), matching well the trend of defect production (see Fig. 4). It has to be compared to the continuous increase in dose (dpa) with time up to the end of the process (see Fig. 6), in spite of an apparent steady state for the chemical bonding within the material at times larger than 9 min. Although we do not have experimental data for electron irradiated graphite, the values reported here for the stored energy compare reasonably well to heat of combustion measurements on neutron-irradiated graphite [58], showing saturation at a similar dose value (0.43 dpa) albeit with an energy level some 45 % larger than predicted here. This is consistent with the fact that collisions with neutrons being more energetic than with electrons, they, on average, create higher energy defects [59] (this is not accounted for in the dose which relates more to the amount of created defects).

A last validation of the structural models concerns the reproduction of electron energy loss (EEL) C K-edge spectra experimentally measured by Mironov *et al.* in a similar *in situ* experiment in the TEM [60]. As the direct calculation of EELS spectra from the large atomistic models simulated in this work is not currently achievable, because of the high computational cost associated with DFT calculations, we adopted a two-stage process: i) firstly we used density functional theory (DFT) to calculate the C K- electron loss near edge structures (ELNES) of a small-scale (216 atoms) model produced by liquid quench MD, and so identified the average contributions

of C_6, C_4, C_{3a} and C_{3b} atom types; and ii) we then produced simulated spectra for the full series of larger scale models based on these separate relative contributions.

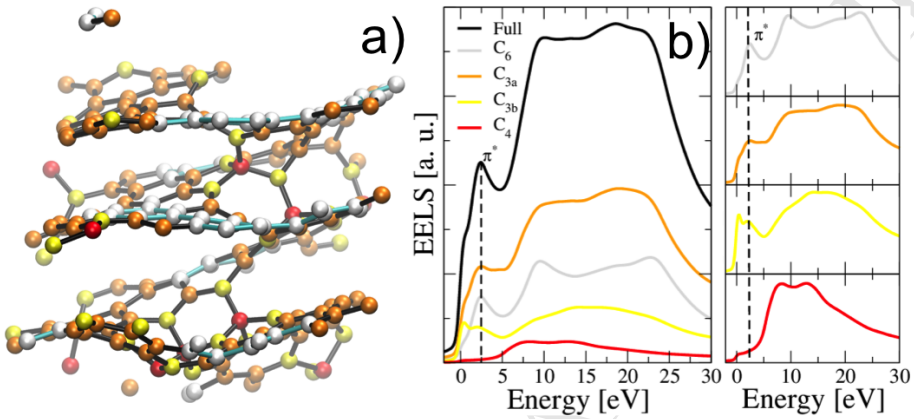

Figure 8: (a) Small scale model of defective graphite produced by liquid quench MD simulation and (b) DFT calculated C K-edge including the individual contributions of C_6, C_{3a}, C_{3b} and C_4 atoms (same color code as Fig. 3).

The small-scale model, shown in Fig. 8(a), contains 29 % C_6, 5 % C_4, 50 % C_{3a} and 16 % C_{3b} atoms, *i.e.*, typical of the values obtained from the large-scale models for irradiation times of 9 min and longer (see Fig. 4). It is worth mentioning that the bonding structure of the model was entirely preserved during the DFT relaxation, confirming the stability of the structure produced with the empirical (AIREBO) potential. Especially, we checked with extra care the stability of the two interlayer sp^3-sp^3 bonds present in the model by testing the local potential energy surface (PES) around these features which closely resemble the well-known "pinch defect" in graphite (*i.e.* interlayer bond between two α atoms) which is known to be artificially stabilized by the AIREBO potential [32]. As shown in the supplementary materials (Fig.

S5), they actually correspond to well-defined minima in the DFT based PES, confirming their stability, at least in sufficiently disordered systems like those corresponding to doses close to 1 dpa.

The C K-ELNES computed from this model using DFT (Fig. 8(b)) is typical of disordered carbons with a narrow, low intensity, π^* band, ≈ 2.5 eV above the Fermi level, and a broad, high intensity σ^* band with maximum intensity in the 7.5-25 eV energy range. Analysis of the contributions from the different carbon environments reveals that: (i) C_4 atoms do not show any π^* features in agreement with experimental diamond C K ELNES [61]; (ii) C_6 atoms have, as for graphite, narrower bands with an increased intensity at the π^* maximum; (iii) C_{3a} atoms show an increase in intensity in the region between the π^* and σ^* bands (the interband intensity); and (iv) C_{3b} atoms show a strong and narrow feature immediately above the Fermi level. The origin of the latter feature, consistent with a well-known edge mode [62] resulting from dangling bonds at the graphene edge, is discussed in the supplementary materials (Fig. S6).

In Fig. 9(a) we compare the EELS spectrum computed for the large-scale irradiated graphite model at the end of the TD-IGAR reconstruction (0.94 dpa) to an experimental spectrum obtained at a similar irradiation dose (1.03 dpa), and observe an overall good agreement, the main deviation being the absence in the experimental spectrum of the low energy shoulder associated to C_{3b} atoms. This can be explained by either the overestimation in the models of the amount of C_4 atoms created by irradition (especially because of the constraint of operating at fixed density), and hence of C_{3b} atoms, or by hydrogen or oxygen passivation of these sites in the actual material.

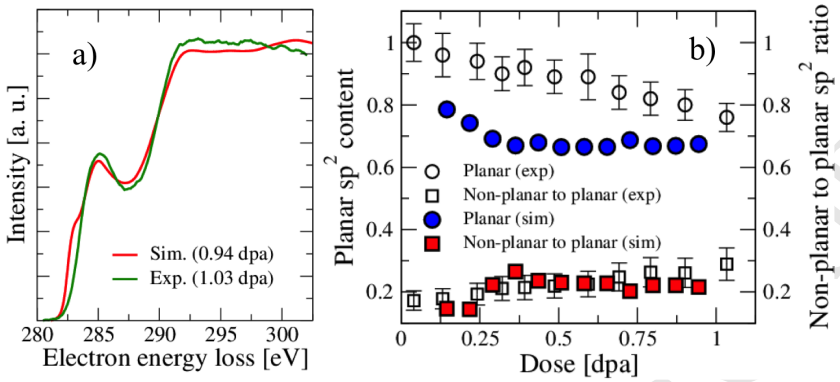

Figure 9: Electron energy loss carbon K-edge spectra. (a) Comparison of the predicted and experimental spectra at ≈ 1 dpa. (b) Evolution with irradiation dose of the absolute planar sp^2 carbon content (circles) and non-planar to planar sp^2 carbon ratio (squares) derived from predicted and experimental spectra. (experimental data are from Mironov *et al.* [60], with the conversion from fluence to dose recalculated based on a displacement energy threshold of 20 eV instead of 30 eV).

However, C_{3b} atoms are stable defects, regularly encounterd in amorphous carbon models produced by ab initio molecular dynamics simulations [63, 64]. From both the simulated and the experimental spectra we have been able to extract and compare the absolute "planar sp^2 carbon content", calculated from the ratio of π^* (band) intensity divided by total integrated intensity, normalized to graphite, and the so-called "non-planar to planar sp^2 carbon ratio" calculated from the ratio of intensity lying between the π^* and σ^* bands (the inter-band intensity) divided by the sum of π^* and inter-band intensities (see Ref. 60). As shown in Fig. 9(b), the experimental decrease in planar sp^2 content and increase in non-planar to planar sp^2 ratio with dose, up to a dose of ≈ 1 dpa at which they are known to plateau [60], are relatively well accounted for by the models, although the predicted plateau

values are obtained at significantly lower doses ($\approx$ 0.35 dpa).

3.4. Prediction of properties

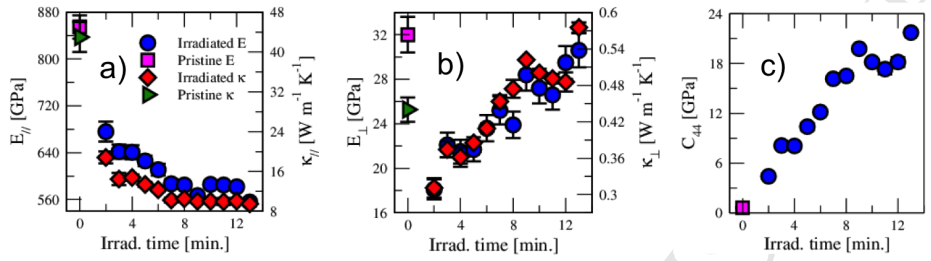

Figure 10: Evolution with irradiation time of (a) the longitudinal and (b) transverse Young's moduli and thermal conductivities as well as of (c) the basal shear elastic constant (C_{44}). Values and error bars of $E_{\parallel}$ and $\kappa_{\parallel}$ for the IGAR models are based on the average values and deviations, respectively, from simulations performed along x and y directions.

Following validation of the models, we present in Fig. 10 some of their elastic constants (the complete list of elastic compliances is given in table S2) and their classical phonon contributions to the thermal conductivity. Interestingly, the evolution of in-plane (Fig. 10(a)) and out-of-plane (Fig. 10(b)) properties show a very similar behavior with increasing irradiation for both the Young's modulus and thermal conductivity. The in-plane modulus, $E_{\parallel}$, quickly drops during the early stages of irradiation, before slowly reaching a plateau at around 560 GPa, accounting for $\approx 2/3$ of the pristine value. Correspondingly, the in-plane conductivity, $\kappa_{\parallel}$, decreases by approximately a factor of four. Out-of-plane properties, $E_{\perp}$ and $\kappa_{\perp}$, progressively increase by a factor of ≈ 2 between 2 and 13 minutes of irradiation (note that the strong reduction in these properties between pristine graphite and the 2 minutes irradiated graphite model is due to the absence of 3D crystalline order in

IGAR reconstructed models [28]). As shown in Fig. 10(c), and in agreement with experimental observations [65] (at much lower damage levels), the most affected elastic constant is C_{44} which increases by a factor of $\approx$ 35 after 13 min of irradiation. The findings reported here can be rationalized by the structural alterations observed in the models: the decrease in in-plane properties is consistent with the decrease of in-plane structural order and the increase in transverse (except between 0 and 2 min of irradiation) and shear properties can be attributed to the progressive development of interlayer covalent bonding [28]. Further discussion of these properties, in line with literature data, is provided in section S4 in the supplementary materials.

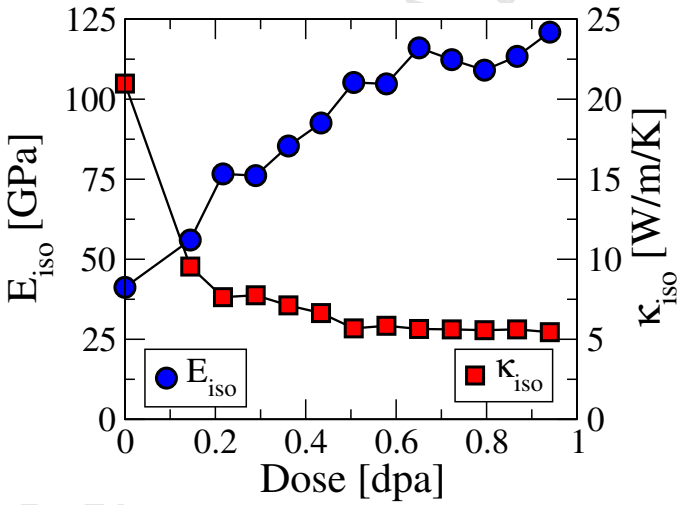

Figure 11: Evolution with dose of the Young's modulus and thermal conductivity homogenized to isotropic graphite (Voigt-Reuss-Hill average).

Finally, we present in Fig. 11 the evolution with irradiation dose of the Young's modulus E_{iso} and thermal conductivity κ_{iso} for a dense isotropic polycrystalline graphite, as a proxy for actual nuclear graphites. This has

been predicted via homogenization of the elastic constants and thermal conductivities computed from the anisotropic irradiated graphite models (see section S5 and Fig. S7 in the supplementary materials). E_{iso} shows the well-known increase in modulus with increasing dose, as well as signs of saturation at around 3 times the value of the virgin material at a dose approaching 1 dpa, in good agreement with experimental observation on neutron irradiated nuclear graphite [5]. Quantitatively speaking, the predicted values of E_{iso} are typically $\approx$ 4 times larger than experimental values for nuclear grade graphite, including the virgin unirradiated material. This is expected as we operate at the density of the single crystal of graphite (2.2 g/cm^3), whilst the density of actual nuclear graphites is usually lower than 1.8 g/cm^3, because of porosity, thus reducing stiffness. The well-known experimental decrease in κ_{iso} with increasing dose [8] is also well accounted for, here by a factor of 4, although a fully quantitative description of thermal conductivity is definitely not achievable using such small (5 nm width) models, as discussed in section S4 in the supplementary materials.

4. Conclusion

We have presented a relatively intuitive and robust methodology to extract the atomistic features of room temperature irradiation damage in graphite solely from HRTEM (002) lattice fringe images. The dynamic reconstructed models have allowed us to characterize damage propagation at doses corresponding to years in a nuclear reactor core and where conventional damage mechanisms, based on Frenkel pair formation and migration, do not apply. The models have been validated via a comparison with experimental data of

dose rate, HRTEM image contrast, EELS carbon K-edges and stored energies. We have demonstrated that these models capture the elastic properties and thermal conductivities of irradiated graphite and, upon homogenization to the case of an isotropic polycrystalline graphite, we are able to predict, for the first time using an atomistic model, the increase in Young's modulus and decrease in thermal conductivity occurring during the irradiation of a nuclear grade graphite. Whilst improvements are possible, for instance by taking into account dimensional changes or using HRTEM images of graphite irradiated with neutrons in the reconstruction procedure, we believe that the approach proposed in this paper opens up many opportunities for the deduction of structure/property diagnostics for irradiated graphite, a particularly relevant issue for current and future graphite-based nuclear power plants.

Acknowledgements

Prof. Malcolm Heggie is gratefully acknowledged by the authors for useful discussions on the manuscript. This work was supported by the french Agence Nationale de la Recherche through the PyroMaN project (grant ANR-2010-BLAN-929), the Materials and System Institute in Bordeaux (Carnot Institute), the UK National Nuclear Laboratory and EPSRC (grants EP/J502042/1 and EP/I002588/1). EPSRC is also acknowledged by TH for a Doctoral Prize Fellowship. JML acknowledges support from the French ICoME2 LabEx (grant ANR-11-LABX-0053). Part of the classical atomistic simulations were performed using the computational resources of the Mésocentre de Calcul Intensif en Aquitaine (MCIA). DFT calculations were carried out on the Advanced Research Computing (ARC2) high perfor-

mance computing facility at the University of Leeds.

References

[1] Tanabe T, Muto S, Gotoh Y, Niwase K. Reduction of the crystalline size of graphite by neutron irradiation. J Nucl Mater. 1990;175(3):258 – 261.

[2] Thrower PA, Reynolds WN. Microstructural changes in neutron-irradiated graphite. J Nucl Mater. 1963;8(2):221–226.

[3] Kelly BT, Marsden BJ, Hall K, Martin DG, Harper A, Blanchard A. Tech. Rep. Ref. TECDOC-1154, IAEA, Vienna. IAEA, Vienna; 2000.

[4] Koike J, Pedraza DF. Dimensional changes in highly oriented pyrolytic graphite due to electron irradiation. J Mater Res. 1994;9(7):1899–1907.

[5] Taylor R, Brown RG, Gilchirst K, Hall E, Hodds AT, Kelly BT, et al. The mechanical properties of reactor graphite. Carbon. 1967;5:519–531.

[6] Burchell TD, Eatherly WP. The effects of radiation damage on the properties of GraphNOL N3M. J Nucl Mater. 1991;179:205 – 208.

[7] Burchell TD. Graphite: Properties and Characteristics. In: Konings RJM, editor. Comprehensive Nuclear Materials. Oxford: Elsevier; 2012. p. 285 – 305.

[8] Snead LL, Burchell TD. Thermal conductivity degradation of graphites due to neutron irradiation at low temperature. J Nucl Mater. 1995;224:222–229.

[9] Telling RH, Ewels CP, El-Barbary AA, Heggie MI. Wigner defects bridge the graphite gap. Nat Mater. 2003;2(5):333–337.

[10] Telling RH, Heggie MI. Radiation defects in graphite. Philos Mag. 2007;87(31):4797–4846.

[11] Bacon GE, Warren BE. X-ray diffraction studies of neutron-irradiated graphite. Acta Cryst. 1956;9(12):1029–1035.

[12] Kelly BT. Graphite - the most fascinating nuclear material. Carbon. 1982;20(1):3–11.

[13] Smith R, Beardmore K. Molecular dynamics studies of particle impacts with carbon-based materials. Thin Sol Films. 1996;272(2):255–270.

[14] Yazyev OV, Tavernelli I, Rothlisberger U, Helm L. Early stages of radiation damage in graphite and carbon nanostructures: A first-principles molecular dynamics study. Phys Rev B. 2007;75:115418.

[15] Chartier A, Van Brutzel L, Pannier B, Baranek P. Atomic scale mechanisms for the amorphisation of irradiated graphite. Carbon. 2015;91:395–407.

[16] Christie HJ, Robinson M, Roach DL, Ross DK, Suarez-Martinez I, Marks NA. Simulating radiation damage cascades in graphite. Carbon. 2015;81:105–114.

[17] Trevethan T, Heggie MI. Molecular dynamics simulations of irradiation defects in graphite: Single crystal mechanical and thermal properties. Comput Mat Sci. 2016;113:60–65.

[18] Jain SK, Pellenq RJM, Pikunic JP, Gubbins KE. Molecular Modeling of Porous Carbons Using the Hybrid Reverse Monte Carlo Method. Langmuir. 2006;22(24):9942–9948.

[19] Bousige C, Ghimbeu CM, Vix-Guterl C, Pomerantz AE, Suleimenova A, Vaughan G, et al. Realistic molecular model of kerogen's nanostructure. Nat Mater. 2016;15(5):576–582.

[20] Petersen TC, Snook IK, Yarovsky I, McCulloch DG, O'Malley B. Curved-Surface Atomic Modeling of Nanoporous Carbon. J Phys Chem C. 2007;111(2):802–812.

[21] Farbos B, Weisbecker P, Fischer HE, Da Costa JP, Lalanne M, Chollon G, et al. Nanoscale structure and texture of highly anisotropic pyrocarbons revisited with transmission electron microscopy, image processing, neutron diffraction and atomistic modelling. Carbon. 2014;80:472–489.

[22] Leyssale JM, Da Costa JP, Germain C, Weisbecker P, Vignoles GL. Structural features of pyrocarbon atomistic models constructed from transmission electron microscopy images. Carbon. 2012;50:4388–4400.

[23] Takeuchi M, Muto S, Tanabe T, Kurata H, Hojou K. Structural change in graphite under electron irradiation at low temperatures. J Nucl Mater. 1999;271–272:280–284.

[24] Karthik C, Kane J, Butt DP, Windes WE, Ubic R. In situ transmission electron microscopy of electron-beam induced damage process in nuclear grade graphite. J Nucl Mater. 2011;412(3):321–326.

[25] Leyssale JM, Da Costa JP, Germain C, Weisbecker P, Vignoles GL. An Image Guided Atomistic Reconstruction of pyrolytic carbons. Appl Phys Lett. 2009;95(23):231912.

[26] Knutsson H. Representing local structure using tensors. In: Proceedings of the 6th Scandinavian Conf. on Image Analysis; 1989. p. 244–251.

[27] Lees AW, Edwards SF. The computer study of transport processes under extreme conditions. J Phys C. 1972;5:1921–9.

[28] Farbos B, Da Costa JP, Vignoles GL, Leyssale JM. Nanoscale elasticity of highly anisotropic pyrocarbons. Carbon. 2015;94:285–294.

[29] Müller-Plathe F. A simple nonequilibrium molecular dynamics method for calculating the thermal conductivity. J Chem Phys. 1997;106:6082–6085.

[30] Brenner DW, Shenderova OA, Harrison JA, Stuart SJ, Ni B, Sinnott SB. A second-generation reactive empirical bond order (REBO) potential energy expression for hydrocarbons. J Phys: Condens Matt. 2002;14(4):783–802.

[31] Leyssale JM, Vignoles GL. A Large-Scale Molecular Dynamics Study of the Divacancy Defect in Graphene. J Phys Chem C. 2014;118(15):8200–8216.

[32] Latham CD, McKenna AJ, Trevethan TP, Heggie MI, Rayson MJ, Briddon PR. On the validity of empirical potentials for simulating radiation damage in graphite: a benchmark. J Physi: Condens Matt. 2015;27(31):316301.

[33] Stuart SJ, Tutein AB, Harrison JA. A reactive potential for hydrocarbons with intermolecular interactions. J Chem Phys. 2000;112(14):6472–6486.

[34] Andersen HC. Molecular dynamics simulations at constant pressure and/or temperature. J Chem Phys. 1980;72:2384.

[35] Berendsen HJC, Postma JPM, van Gunsteren WF, DiNola A, Haak JR. Molecular Dynamics with Coupling to an External Bath. J Chem Phys. 1984;81:3684–3690.

[36] Kilaas R. Interactive software for simulation of high resolution TEM images. In: Geiss RH, editor. Proceedings of the 22nd Annual Conference of the Microbeam Aanalysis Society; 1987. p. 293–300.

[37] Hohenberg P, Kohn W. Inhomogeneous electron gas. Phys Rev. 1964;136:B864.

[38] Kohn W, Sham LJ. Self-consistent equations including exchange and correlation effects. Phys Rev. 1965;140:A14433.

[39] Clark SJ, Segall MD, Pickard CJ, Hasnip PJ, Probert MJ, Refson K, et al. First principles methods using CASTEP. Z Kristallogr. 2005;220:567.

[40] Tkatchenko A, Scheffler M. Accurate molecular van der Waals interactions from ground-state electron density and free-atom reference data. Phys Rev Lett. 2009;102:073005.

[41] Perdew JP, Burke K, Ernzerhof M. Generalized Gradient Approximation Made Simple. Phys Rev Lett. 1996;77:3865–8.

[42] Monkhorst HJ, Pack JD. Special points for Brillouin-zone integrations. Phys Rev B. 1976;13:5188–5192.

[43] Pickard CJ, Payne M. In: Rodenburg JM, editor. Ab Initio EELS: Beyond the Fingerprint. Philadelphia, PA: IOP Publishing LTD; 1997. p. 175.

[44] Blöchl PE. Projector augmented-wave method. Phys Rev B. 1994;50:17953–17979.

[45] Krause MO. Atomic radiative and radiationless yields for K and L shells. J Phys Chem Ref Data. 1979;8:307–327.

[46] Huang PY, Ruiz-Vargas CS, van der Zande AM, Whitney WS, Levendorf MP, Kevek JW, et al. Grains and grain boundaries in single-layer graphene atomic patchwork quilts. Nature. 2011;469:389–392.

[47] Suarez-Martinez I, Savini G, Haffenden G, Campanera JM, Heggie MI. Dislocations of Burgers vector c /2 in graphite. Phys Stat Sol (c). 2007;4(8):2958–2962.

[48] Trevethan T, Dyulgerova P, Latham CD, Heggie MI, Seabourne CR, Scott AJ, et al. Extended Interplanar Linking in Graphite Formed from Vacancy Aggregates. Phys Rev Lett. 2013;111:095501.

[49] Da Costa JP, Weisbecker P, Farbos B, Leyssale JM, Vignoles GL, Ger-

main C. Investigating carbon materials nanostructure using image orientation statistics. Carbon. 2015;84:160–173.

[50] McKenna AJ, Trevethan T, Latham CD, Young PJ, Heggie MI. Threshold displacement energy and damage function in graphite from molecular dynamics. Carbon. 2016;99:71–78.

[51] Krasheninnikov AV, Banhart F, Li JX, Foster AS, Nieminen RM. Stability of carbon nanotubes under electron irradiation: Role of tube diameter and chirality. Phys Rev B. 2005;72:125428.

[52] Banhart F. Irradiation effects in carbon nanostructures. Rep Prog Phys. 1999;62:1181–1221.

[53] Banhart F, Füller T, Redlich P, Ajayan PM. The formation, annealing and self-compression of carbon onions under electron irradiation. Chem Phys Lett. 1997;269(3):349–355.

[54] Zobelli A, Gloter A, Ewels CP, Seifert G, Colliex C. Electron knock-on cross section of carbon and boron nitride nanotubes. Phys Rev B. 2007;75:245402.

[55] Susi T, Hofer C, Argentero G, Leuthner GT, Pennycook TJ, Mangler C, et al. Isotope analysis in the transmission electron microscope. Nat Commun. 2016;7:13040.

[56] Oen O. Cross Sections for Atomic Displacements in Solids by Fast Electrons; Tech. rep., Oak Ridge National Lab; 1965.

[57] Kotakoski J, Santos-Cottin D, Krasheninnikov AV. Stability of Graphene Edges under Electron Beam: Equilibrium Energetics versus Dynamic Effects. ACS Nano. 2012;6:671–676.

[58] Nightingale RE. Nuclear Graphite. Academic Press; 1962.

[59] Krasheninnikov AV, Nordlund K. Ion and electron irradiation-induced effects in nanostructured materials. J App Phys. 2010;107:071301.

[60] Mironov BE, Freeman HM, Brown AP, Hage FS, Scott AJ, Westwood AVK, et al. Electron irradiation of nuclear graphite studied by transmission electron microscopy and electron energy loss spectroscopy. Carbon. 2015;83:106–117.

[61] Mykhaylyk OO, Solonin YM, Batchelder DN, Brydson R. Transformation of nanodiamond into carbon onions: A comparative study by high-resolution transmission electron microscopy, electron energy-loss spectroscopy, x-ray diffraction, small-angle x-ray scattering, and ultraviolet Raman spectroscopy. J Appl Phys. 2005;97(7):074302.

[62] Suenaga K, Koshino M. Atom-by-atom spectroscopy at graphene edge. Nature. 2010;468(7327):1088–1090.

[63] Marks NA, McKenzie DR, Pailthorpe BA, Bernasconi M, Parrinello M. Microscopic Structure of Tetrahedral Amorphous Carbon. Phys Rev Lett. 1996;76:768–771.

[64] Martin N, Pailler R, Leyssale JM. Carbon-ceramic (AlN) interfaces from liquid quench ab initio molecular dynamics simulations. Mol Simul. 2014;40:160–168.

[65] Seldin EJ, Nezbeda CW. Elastic constants and electron-microscope observations of neutron-irradiated compression-annealed pyrolytic and single-crystal graphite. J Appl Phys. 1970;41:3389–3400.